

# Multiple sulfur isotopic reservoirs in the Moon and implications for the evolution of planetary interiors

Samantha Faircloth (✉ [samantha.faircloth@open.ac.uk](mailto:samantha.faircloth@open.ac.uk))

The Open University

**Mahesh Anand**

The Open University <https://orcid.org/0000-0003-4026-4476>

**Ian Franchi**

The Open University <https://orcid.org/0000-0003-4151-0480>

**Xuchao Zhao**

The Open University <https://orcid.org/0000-0003-0268-8139>

**Sara Russell**

The Natural History Museum <https://orcid.org/0000-0001-5531-7847>

---

## Article

**Keywords:** sulfur isotopic reservoirs, planetary interiors, moon, lunar interior

**Posted Date:** September 2nd, 2020

**DOI:** <https://doi.org/10.21203/rs.3.rs-66943/v1>

**License:**  This work is licensed under a Creative Commons Attribution 4.0 International License.

[Read Full License](#)

---



22 Very few *in situ* lunar sulfur studies exist, with the major focus being on bulk-rocks in which  
23 a relatively restricted sulfur isotope fractionation is observed, leading to suggestions that the  
24 source of sulfur in the lunar interior is homogeneous. Using a novel approach, we present for  
25 the first time two complementary datasets combining *in situ* secondary ion mass spectrometry  
26 and X-ray absorption near-edge structure spectroscopy of lunar apatite, to investigate the late-  
27 stage behaviour of sulfur in lunar basaltic melts. Our measurements reveal varied sulfur  
28 contents of ~20–2,800 ppm and  $\delta^{34}\text{S}$  values of  $-33.3 \pm 3.8\%$  to  $+36.4 \pm 3.2\%$  ( $2\sigma$ ). The  
29 apatites have  $\text{S}^{6+}/\Sigma\text{S}_{\text{tot}}$  ratios of  $>0$ , with average values as high as 0.55, providing evidence  
30 for the existence of relatively oxidized late-stage silicate melts on the Moon. We propose the  
31 existence of multiple, and previously unrecognised, distinct sulfur isotopic reservoirs in the  
32 lunar interior and atypical oxidizing conditions in late-stage silicate melts. These findings are  
33 important for our understanding of lunar formation processes and the evolution of redox  
34 conditions during the formation of terrestrial bodies.

35  
36 Redox conditions played a crucial role in the evolution and chemical differentiation of  
37 planetary bodies in the early Solar System<sup>1</sup>. When compared with terrestrial basalts, lunar  
38 (mare) basalts formed under conditions that were significantly more reducing, which is  
39 evidenced by the presence of ubiquitous metallic iron (Fe) in lunar rocks<sup>2</sup>. The primary S-  
40 bearing mineral phase in mare basalts is late-stage crystallising troilite (FeS), which contains  
41 the more reduced form of sulfur<sup>3</sup>. In magmatic systems, S exists in many phases (e.g. a melt  
42 or a gas), in multiple-oxidation states (predominantly, sulfide ( $\text{S}^{2-}$ ) and sulfate ( $\text{S}^{6+}$ )) and it  
43 has many stable isotopes (e.g.,  $^{32}\text{S}$ ,  $^{33}\text{S}$  and  $^{34}\text{S}$ ) (refs. <sup>4,5</sup>). Earlier studies of mare basalts  
44 reported  $\delta^{34}\text{S}$  values of  $-5.2\%$  to  $+1.44\%$  from bulk-rocks<sup>6-13</sup>, whereas a more recent study  
45 documented very restricted  $\delta^{34}\text{S}$  values between  $+0.44\%$  and  $+0.69\%$  for ten mare basalt  
46 bulk-rocks, suggesting an initially homogeneous source for sulfur<sup>14</sup>. However, *in situ*

47 measurements of ‘vein and replacement troilite’ (FeS) from Apollo 16 lunar highlands  
48 clasts<sup>15</sup> have negative  $\delta^{34}\text{S}$  values of  $-3.3 \pm 1.6\text{‰}$  to  $-1.0 \pm 1.6\text{‰}$  ( $2\sigma$ ) which are partly  
49 attributed to secondary alteration by a  $^{32}\text{S}$ -enriched vapour phase. Likewise, Apollo 17  
50 volcanic glass beads have negative  $\delta^{34}\text{S}$  values ( $-2.62\text{‰}$  to  $-0.19\text{‰}$ ) owing to the initial loss  
51 of  $^{32}\text{S}$  to the vapour phase during extrusive volcanism, followed by incomplete and variable  
52  $^{32}\text{S}$  condensation from the vapour cloud onto the bead surfaces<sup>16</sup>. With the exception of one  
53 *in situ* study that reports a positive average  $\delta^{34}\text{S}$  value of  $+10.5 \pm 3.0\text{‰}$  ( $2\sigma$ ) from  
54 measurements of a single grain<sup>17</sup>, the S isotopic composition of lunar apatite, so far, remains  
55 unstudied despite its potential to shed light on the nature of S isotopic reservoir(s) in the  
56 Moon. With a general chemical formula of  $\text{Ca}_5(\text{PO}_4)_3(\text{F},\text{Cl},\text{OH})$  apatite is a late-stage  
57 crystallising mineral in a basaltic melt that is capable of hosting volatile elements, including  
58 S within its crystal structure<sup>18-20</sup>. Terrestrial apatite  $\delta^{34}\text{S}$  values are positive ( $1.0\text{‰}$  to  $8.5\text{‰}$ )  
59 due to ascent-driven degassing and the presence of multiple oxidation states of sulfur (most  
60 likely  $\text{S}^{6+}$  and  $\text{S}^{2-}$ ) in the magmas<sup>21</sup>. Apatite is sensitive to S oxidation state changes in the  
61 silicate melt and would preferentially incorporate  $\text{S}^{6+}$  into its crystal structure<sup>19,22,23</sup>.  
62 Accordingly, otherwise undetectable quantities of  $\text{S}^{6+}$  present in a reduced silicate melt can  
63 be detected and measured in apatite<sup>23</sup>. The results of recent X-ray absorption near-edge  
64 structure (XANES) spectroscopy<sup>24</sup> of lunar apatites in two Apollo basalt samples demonstrate  
65 the dominance of  $\text{S}^{2-}$ , and relatively low oxygen fugacity ( $f\text{O}_2$ ) of lunar magmas, where more  
66 than half of the measurements have a  $\text{S}^{6+}/\Sigma\text{S}_{\text{tot}}$  ratio of  $<0.03$ .  
67 We analysed S in apatites of thirteen Apollo samples to investigate S isotopic reservoir(s) in  
68 the lunar interior and the potential of apatite to reveal the  $f\text{O}_2$  of the late-stage silicate melt.  
69 Chlorine abundance and isotopes were simultaneously measured with S to better understand  
70 the unknown behaviour of S from what is already known for Cl in lunar apatite in relation to  
71 the identification of distinctive Cl isotopic reservoirs in the Moon.

72

### 73 **Sulfur in lunar apatite**

74 The abundances and isotopic compositions of S and Cl were measured on the same spot in  
75 apatite grains from ten mare basalts, a KREEP-rich basalt, a feldspathic polymict breccia and  
76 a feldspathic granulitic impactite (Supplementary Information), using a newly adapted  
77 protocol for the Cameca 50L nano-scale secondary ion mass spectrometer (NanoSIMS)  
78 (Methods) at the Open University. The S analysis of lunar apatites reveal ~20–2,800 ppm S  
79 with S isotope ( $\delta^{34}\text{S}_{\text{(V-CDT)}}$ ) values ranging from  $-33.3 \pm 3.8\text{‰}$  to  $+36.4 \pm 3.2\text{‰}$  ( $2\sigma$ ),  
80 representing significant variability (Figure 1 and Supplementary Information). There is a lack  
81 of any statistically significant correlation between  $\delta^{34}\text{S}$  and  $\delta^{37}\text{Cl}$  (Supplementary  
82 Information), which we interpret as a decoupling of S and Cl during the evolution of the lunar  
83 interior. Consequently, the trend of increasing  $\delta^{37}\text{Cl}$  in apatites from mare basalts through to  
84 KREEP basalts through to highlands rocks that tells a story of the evolution of Cl in the lunar  
85 interior<sup>25-30</sup>, is not apparent in the  $\delta^{34}\text{S}$  dataset.

86 Sulfur is heterogeneously distributed in lunar apatites, with two orders of magnitude  
87 difference between the lowest and the highest S abundances and a difference of ~70%  
88 separating the minimum and maximum  $\delta^{34}\text{S}$  values. There are no obvious correlations among  
89 the samples in terms of S abundances and  $\delta^{34}\text{S}$  values. There are, however, three distinct  
90 clusters of S isotopic compositions: one with anomalously high  $\delta^{34}\text{S}$  values, one with  
91 anomalously low  $\delta^{34}\text{S}$  values and one straddling 0‰, covering a region of ~ +10‰ to ~ -10‰  
92 (Figure 1 and Supplementary Information). When compared with the  $\delta^{34}\text{S}$  values of a single  
93 lunar apatite in granulitic impactite sample 79215 ( $+9.7 \pm 2.8\text{‰}$  and  $+11.3 \pm 3\text{‰}$  ( $2\sigma$ ))<sup>17</sup>, the  
94 results of our measurements on six apatite grains of the same sample are, within statistical  
95 uncertainty, identical (Supplementary Information). Overall, our results show that lunar  
96 apatites appear to have a far greater spread in  $\delta^{34}\text{S}$  compared with the very restricted mare

97 basalt bulk-rock values of +0.44‰ to +0.69‰ (ref. <sup>14</sup>). Given that the primary S-bearing  
98 mineral phase in mare basalts is troilite<sup>3</sup> which forms after apatite and exists in varying  
99 abundances in every Apollo sample analysed in this study, it is likely that the more restricted  
100 bulk-rock values (+0.44‰ to +0.69‰) predominantly reflect the  $\delta^{34}\text{S}$  value of troilite, which  
101 masks the S contribution from apatite (Supplementary Information).

102

### 103 **Sulfur degassing and vapour phase interaction**

104 Studies indicate that sulfur isotope compositions may be affected by redox processes<sup>21,31-33</sup>.  
105 The apatites in low-Ti basalt 15065 have the lowest  $\delta^{34}\text{S}$  values ( $-33.3 \pm 3.8\%$  to  $-14.1 \pm$   
106  $2.6\%$ ) measured in this study (Figure 1 and Supplementary Information). In this sample,  
107 there is a positive correlation between apatite  $\delta^{34}\text{S}$  and S abundance. Moreover, there is a  
108 core-rim decrease of both  $\delta^{34}\text{S}$  ( $-18.0 \pm 2.4\%$  to  $-27.4 \pm 6.5\%$ ) and S abundance ( $\sim 1,500$  ppm  
109 to  $\sim 410$  ppm) in a single zoned apatite grain in this sample. We interpret this as a loss of the  
110 heavier S isotope during degassing (e.g. ref. <sup>34</sup>) from a reduced ( $\text{S}^{2-}$ -rich) late-stage silicate  
111 melt, whereby the lighter S isotope is preferentially retained in the melt<sup>21,31,32,35</sup>. We propose  
112 that, prior to apatite crystallisation, the late-stage degassing species was isotopically heavy  
113  $\text{H}_2\text{S}$  and  $\text{SO}_2$  which degassed near to the surface of the Moon (e.g. refs. <sup>35,36</sup>). The apatites in  
114 15065 show no signs of secondary alteration but are zoned with respect to S (Supplementary  
115 Information) which is suggestive of primary crystal growth within a silicate magma.  
116 However, given the anomalously low  $\delta^{34}\text{S}$  values for apatites in sample 15065, in addition to  
117 S isotope fractionation from degassing, we conclude that the late-stage silicate melt interacted  
118 with a reduced and already fractionated (with respect to S isotopes) vapour phase prior to or  
119 during apatite crystallisation (after  $>95\%$  crystallisation (e.g. refs. <sup>37,38</sup>)).  
120 The apatites of low-Ti basalt 15016 have the highest  $\delta^{34}\text{S}$  values recorded in this study ( $+28.9$   
121  $\pm 8.3\%$  to  $+36.4 \pm 3.2\%$ ). The anomalous  $\delta^{34}\text{S}$  signature may be attributed to increased

122 oxidation as a result of interaction between a relatively oxidized vapour phase and the late-  
123 stage silicate melt. A more oxidised late-stage silicate melt would predominantly contain S<sup>6+</sup>  
124 dissolved as SO<sub>4</sub><sup>2-</sup>. This melt can preferentially retain <sup>34</sup>S (refs. <sup>21,33</sup>), leading to degassing of  
125 isotopically light H<sub>2</sub>S and SO<sub>2</sub>, leaving behind a heavier δ<sup>34</sup>S signature in the residual silicate  
126 melt prior to apatite crystallisation.

127 Whilst unexpected, the existence of transient oxidized conditions in the lunar environment  
128 have been reported following the discovery of Fe-oxide (Fe<sup>3+</sup>) in a breccia clast<sup>39</sup> and  
129 volcanic glass beads<sup>40</sup>. The variation of S abundance between apatites likely indicates  
130 crystallisation at slightly different stages, where the smallest fraction of silicate melt  
131 remaining would have contained the highest concentration of S. This is clearly demonstrated  
132 by a single zoned apatite grain which has a core-rim increase of S abundance (~1,210 to  
133 ~2,760 ppm S) that coincides with crystal growth in the melt (Supplementary Information).  
134 Our results highlight the existence of multiple, distinct, sulfur isotopic reservoirs with  
135 different levels of oxidation in the lunar crust that have not previously been identified. These  
136 distinct sources represent heterogeneity in the lunar crust and, therefore, in lunar basaltic  
137 melts. This was likely to have been caused by heat-inducing remobilisation of elements in  
138 different magmatic lithologies of the lunar crust (e.g. ref. <sup>15</sup>). When compared with the  
139 silicate melt from which apatite crystallised, the mobile vapour phases interacted to a lesser  
140 degree with the segregated immiscible sulfide melt (Supplementary Information) from which  
141 troilite formed.

142

### 143 **The sulfur oxidation state of lunar apatite**

144 In order to further constrain which species of S was a dominant component in the late-stage  
145 silicate melts, we measured the oxidation state of S in lunar apatite with μ-XANES  
146 spectroscopy at the S K-edge on beamline I18 at Diamond Light Source, UK (Methods). We

147 analysed twelve different apatite grains from five Apollo mare basalts, along with  
148 surrounding mineral phases (e.g. pyroxene and glass), a terrestrial apatite (Durango) and  
149 reference materials with known S oxidation states. The full S-XANES spectroscopy results  
150 are provided in the Supplementary Information. The results of this study show that the more  
151 oxidized state of sulfur ( $S^{6+}$ ) is present in every lunar apatite analysed, with all having  
152  $S^{6+}/\Sigma S_{\text{tot}}$  ratios of  $>0$ . To preserve the  $\delta^{34}\text{S}$  signature, the majority of apatites crystallised after  
153 the main phase of S degassing and, therefore, the estimated  $f\text{O}_2$  of the silicate melt represents  
154 the time at or during which apatites crystallised<sup>41,42</sup>. The existence of the more oxidized  $S^{6+}$  in  
155 lunar apatite implies atypical oxidizing conditions at the time of their crystallisation.  
156 S-XANES spectroscopy of low-Ti basalt 12039 was performed by Brounce et al.<sup>24</sup> who  
157 reported  $S^{6+}/\Sigma S_{\text{tot}}$  ratios between 0 and 0.45 across six lunar apatite grains. The apatite  
158 analyses resulting in  $S^{6+}/\Sigma S_{\text{tot}}$  ratios of  $>0.03$  were attributed to the presence of fractures and/  
159 or pits that were thought not to represent primary S of apatite but secondary alteration and  
160 oxidation<sup>24</sup>. However, our analysis of a different thin section of the same sample reveals  
161  $S^{6+}/\Sigma S_{\text{tot}}$  ratios between 0.23 and 0.42 for measurements made in crack-free regions of two  
162 different apatite grains, highlighting measurable contents of indigenous  $S^{6+}$ . Low-Ti basalt  
163 15016 is the only sample analysed with S-XANES spectroscopy that has apatites with  
164 exclusively positive  $\delta^{34}\text{S}$  values which we interpreted to have crystallised from a relatively  
165 oxidized late-stage silicate melt dominated by  $S^{6+}$ . Further evidence for this comes from an  
166 apatite grain in this sample that has an average  $S^{6+}/\Sigma S_{\text{tot}}$  ratio of 0.55 (Figure 2), where  $\sim 65\%$   
167 of the S-XANES measurements have  $S^{6+}/\Sigma S_{\text{tot}}$  ratios of  $>0.5$  (Supplementary Information).  
168 Conversely, five apatites in low-Ti basalt samples 15058 and 15065 analysed with S-XANES  
169 spectroscopy have, within statistical uncertainty, negative  $\delta^{34}\text{S}$  values that are consistent with  
170 loss of  $^{34}\text{S}$  from a reduced ( $S^{2-}$ ) silicate melt. These apatites have average  $S^{6+}/\Sigma S_{\text{tot}}$  values  
171 between 0.25 and 0.36 (Figure 2) which, alongside the S isotope data, provides additional

172 evidence of the dominance of S<sup>2-</sup> in the late-stage silicate melt at the time of apatite  
173 crystallisation (Figure 3).  
174 The *in situ* S measurements of apatite have revealed the existence of distinct, and previously  
175 unrecognized, S isotopic reservoirs in the lunar interior. Unlike the Earth, the Moon is  
176 practically devoid of alteration processes induced by active plate tectonics or a hydrological  
177 or biological cycle and, therefore, observations of this study have universal implications,  
178 whereby the Moon provides a unique insight into the evolutionary processes of inner Solar  
179 System planetary bodies.  
180 By combining the NanoSIMS and S-XANES datasets, this novel study demonstrates that the  
181 S species in the late-stage silicate melt and, therefore, the S species that was degassed, was  
182 dictated by the S oxidation state of the melt. Our findings call into question the applicability  
183 of standard reducing conditions to lunar late-stage silicate melts. Apatites show evidence of  
184 having crystallised under atypical lunar conditions following the interaction between melts  
185 and vapour phases originating from distinct S isotopic reservoirs that either contain or are  
186 dominated by the more oxidized form of S. These findings have significant implications for  
187 our understanding of lunar formation processes and suggest that variations in oxidation state  
188 may be an inevitable process in planetary igneous evolution.

189

## 190 **Acknowledgements**

191 This work was supported by a UK Science and Technology Facilities Council (STFC)  
192 Studentship to S.J.F., a UK STFC grant (# ST/P000657/1 to M.A. and I.A.F.) and by the  
193 Open University Space Strategic Research Area (SRA). We thank the curatorial staff at  
194 NASA Johnson Space Centre for allocations of Apollo samples for this study; Tina Geraki  
195 for support with beamline (I18) operations at Diamond Light Source, UK; and Richard C.

196 Greenwood and Peter Landsberg at The Open University for invaluable observations and  
197 laboratory support.

198

### 199 **Author Contributions**

200 M.A., I.A.F. conceived the project and together with S.J.F. designed the work plan. S.J.F. led  
201 all of the data collection with help from X.Z. and I.A.F. (NanoSIMS) and from M.A. and  
202 I.A.F. (S-XANES). Data reduction was undertaken by S.J.F. All authors contributed to the  
203 writing, discussions and revision of the manuscript.

204

### 205 **Competing Interests statement**

206 The authors declare no competing interests.

207

### 208 **References**

209

- 210 1. Deng, J., Du, Z., Karki, B. B., Ghosh, D. B. & Lee, K. K. M. A magma ocean origin to  
211 divergent redox evolutions of rocky planetary bodies and early atmospheres. *Nat.*  
212 *Commun.* **11**, 1-7 (2020).
- 213
- 214 2. Taylor, G. J. et al. . in *Lunar Sourcebook: A User's Guide to the Moon* (eds Heiken, G.,  
215 Vaniman, D. T. & French, B. M.) 183-284 (Cambridge University Press, 1991).
- 216
- 217 3. Haskin, L. A. & Warren, P. H. in *Lunar Sourcebook: A User's Guide to the Moon* (eds  
218 Heiken, G., Vaniman, D. T. & French, B. M.) 357–474 (Cambridge University Press,  
219 1991).

220

- 221 4. Métrich, N., Berry, A. J., O'Neill, H. S. C. & Susini, J. The oxidation state of sulfur in  
222 synthetic and natural glasses determined by X-ray absorption spectroscopy. *Geochim.*  
223 *Cosmochim. Acta* **73**, 2382-2399 (2009).
- 224
- 225 5. Criss, R. E. & Farquhar, J. Abundance, notation, and fractionation of light stable isotopes.  
226 *Rev. in Mineral. Geochem.* **68**, 15-30 (2008).
- 227
- 228 6. Thode, H. G & Rees, C. E. Measurement of sulphur concentrations and the isotope ratios  
229  $^{33}\text{S}/^{32}\text{S}$ ,  $^{34}\text{S}/^{32}\text{S}$  and  $^{36}\text{S}/^{32}\text{S}$  in Apollo 12 samples. *Earth Planet. Sci. Lett.* **12**, 434-438  
230 (1971).
- 231
- 232 7. Thode, H. G & Rees, C. E. in *The Apollo 15 Lunar Samples* (eds Chamberlain, J. W. &  
233 Watkins, C.) 402–403 (Lunar Science Institute, 1972).
- 234
- 235 8. Rees, C. E. & Thode, H. G. Sulphur concentrations and isotope ratios in lunar samples.  
236 *Proc. 3<sup>rd</sup> Lunar Planet. Sci. Conf.* **3**, 1479-1485 (1972).
- 237
- 238 9. Rees, C. E. & Thode, H. G. Sulphur concentrations and isotope ratios in Apollo 16 and 17  
239 samples. *Proc. 5<sup>th</sup> Lunar Planet. Sci. Conf.* **2**, 1963-1973 (1974).
- 240
- 241 10. Petrowski, C., Kerridge, J. F. & Kaplan, I. R. Light element geochemistry of the Apollo  
242 17 site. *Proc. 5<sup>th</sup> Lunar Planet. Sci. Conf.* **2**, 1939-1948 (1974).
- 243

- 244 11. Gibson, E. K. Jr., Chang, S., Lennon, K., Moore, G. W. & Pearce, G. W. Sulfur  
245 abundances and distributions in mare basalts and their source magmas. *Proc. 6<sup>th</sup> Lunar*  
246 *Planet. Sci. Conf.* **2**, 1287-1301 (1975).  
247
- 248 12. Kaplan, I. R., Kerridge, J. F. & Petrowski, C. Light element geochemistry of the Apollo  
249 15 site. *Proc. 7th Lunar Planet. Sci. Conf.* **1**, 481-492 (1976).  
250
- 251 13. Des Marais, D. J. D. Light element geochemistry and spallogensis in lunar rocks.  
252 *Geochim. Cosmochim. Acta* **47**, 1769-1781 (1983).  
253
- 254 14. Wing, B. A. & Farquhar, J. Sulfur isotope homogeneity of lunar mare basalts. *Geochim.*  
255 *Cosmochim. Acta* **170**, 266-280 (2015).  
256
- 257 15. Shearer, C. K. et al. Origin of sulfide replacement textures in lunar breccias. Implications  
258 for vapor element transport in the lunar crust. *Geochim. Cosmochim. Acta* **83**, 138–158  
259 (2012).  
260
- 261 16. Ding, T. P., Thode, H. G. & Rees, C. E. Sulphur content and sulphur isotope composition  
262 of orange and black glasses in Apollo 17 drive tube 74002/1. *Geochim. Cosmochim. Acta*  
263 **47**, 491-496 (1983).  
264
- 265 17. Treiman, A. H. et al. Phosphate-halogen metasomatism of lunar granulite 79215: Impact-  
266 induced fractionation of volatiles and incompatible elements. *Am. Mineral.* **99**, 1860-1870  
267 (2014).  
268

- 269 18. Papike, J., Taylor, L. & Simon, S. in *Lunar Sourcebook: A User's Guide to the Moon* (eds  
270 Heiken, G., Vaniman, D. T. & French, B. M.) 121-181 (Cambridge Univ. Press, 1991).  
271
- 272 19. Peng, G., Luhr, J. F. & McGee, J. J. Factors controlling sulfur concentrations in volcanic  
273 apatite. *Am. Mineral.* **82**, 1210–1224 (1997).  
274
- 275 20. Hughes, J. M. & Rakovan, J. F. Structurally robust, chemically diverse: Apatite and  
276 apatite supergroup minerals. *Elements* **11**, 165-170 (2015).  
277
- 278 21. Economos, R., Boehnke, P. & Burgisser, A. Sulfur isotopic zoning in apatite crystals: A  
279 new record of dynamic sulfur behavior in magmas. *Geochim. Cosmochim. Acta* **215**, 387-  
280 403 (2017).  
281
- 282 22. Parat, F., Holtz, F. & Streck, M. J. in *Sulfur in Magmas and Melts: Its Importance for*  
283 *Natural and Technical Processes* (eds Behrens, H. & Webster, J. D.) 285-314 (Reviews  
284 in Mineralogy and Geochemistry 73, Mineralogical Society of America, 2011).  
285
- 286 23. Konecke, B. A., Fiege, A., Simon, Linsler, S. & Holtz, F. An experimental calibration of  
287 a sulfur-in-apatite oxybarometer for mafic systems. *Geochim. Cosmochim. Acta* **265**, 242-  
288 258 (2019).  
289
- 290 24. Brounce, M. et al. The oxidation state of sulfur in lunar apatite. *Am. Mineral.* **104**, 307–  
291 312 (2019).  
292

- 293 25. Barnes, J. J., Franchi, I., McCubbin, F. M. & Anand, M. Multiple reservoirs of volatiles in  
294 the Moon revealed by the isotopic composition of chlorine in lunar basalts. *Geochim.*  
295 *Cosmochim. Acta* **266**, 144-162 (2019).
- 296
- 297 26. Boyce, J. W. et al. Early loss, fractionation, and redistribution of chlorine in the Moon as  
298 revealed by the low-Ti lunar mare basalt suite. *Earth Planet. Sci. Lett.* **500**, 205–214 (2018).
- 299
- 300 27. Barnes, J. J. et al. Early degassing of lunar urKREEP by crust-breaching impact(s). *Earth*  
301 *Planet. Sci. Lett.* **447**, 84-94 (2016).
- 302
- 303 28. Boyce, J. W. et al. The chlorine isotope fingerprint of the lunar magma ocean. *Sci. Adv.* **1**,  
304 1-8 (2015).
- 305
- 306 29. McCubbin, F. M. et al. Magmatic volatiles (H, C, N, F, S, Cl) in the lunar mantle, crust,  
307 and regolith: Abundances, distributions, processes, and reservoirs. *Am. Mineral.* **100**,  
308 1668-1707 (2015).
- 309
- 310 30. Tartèse, R. et al. Apatites in lunar KREEP basalts: The missing link to understanding the  
311 H isotope systematics of the Moon. *Geology* **42**, 363-366 (2014).
- 312
- 313 31. Harrison, A. & Thode, H. The kinetic isotope effect in the chemical reduction of sulphate.  
314 *Trans. Faraday* **53**, 1648-1651 (1957).
- 315
- 316 32. Sakai, H. & Nagasawa, H. Fractionation of sulfur isotopes in volcanic gases. *Geochim.*  
317 *Cosmochim. Acta* **15**, 32-39 (1958).

318

319 33. Ohmoto, H. & Rye, R. O. in *Geochemistry of hydrothermal ore deposits* (ed Barnes, H.  
320 L.) 509-567 (John Wiley and Sons, Inc., 1979).

321

322 34. Saal, A. E. et al. Volatile content of lunar volcanic glasses and the presence of water in  
323 the Moon's interior. *Nature* **454**, 192-195 (2008).

324

325 35. de Moor, J. M. Sulfur degassing at Erta Ale (Ethiopia) and Masaya (Nicaragua)  
326 volcanoes: Implications for degassing processes and oxygen fugacities of basaltic  
327 systems. *Geochem. Geophys. Geosyst.* **14**, 4076-4108 (2013).

328

329 36. Marini, L., Moretti, R. & Accornero, M. in *Sulfur in Magmas and Melts: Its Importance*  
330 *for Natural and Technical Processes* (eds Behrens, H. & Webster, J. D.) 423-292  
331 (Reviews in Mineralogy and Geochemistry 73, Mineralogical Society of America, 2011).

332

333 37. Sha, L. K. Whitlockite solubility in silicate melts: some insights into lunar and planetary  
334 evolution. *Geochim. Cosmochim. Acta* **64**, 3217–3236 (2000).

335

336 38. Tartèse, R. & Anand, M. Late delivery of chondritic hydrogen into the lunar mantle:  
337 Insights from mare basalts. *Earth Planet. Sci. Lett.* **361**, 480-486 (2013).

338

339 39. Joy, K. H. et al. Identification of magnetite in lunar regolith breccia 60016: Evidence for  
340 oxidized conditions at the lunar surface. *Meteorit. Planet. Sci.* **50**, 1157–1172 (2015).

341

- 342 40. McCanta, M. C. et al. *In situ* measurement of ferric iron in lunar glass beads using Fe-  
343 XAS. *Icarus* **285**, 95-102 (2017).
- 344
- 345 41. Konecke, B. A., Fiege, A., Simon, A. C., Parat, F. & Stechern, A. Co-variability of  $S^{6+}$ ,  
346  $S^{4+}$ , and  $S^{2-}$  in apatite as a function of oxidation state: Implications for a new  
347 oxybarometer. *Am. Mineral.* **102**, 548–557 (2017).
- 348
- 349 42. Kim, Y., Konecke B., Fiege, A., Simon, A. & Becker, U. An ab-initio study of the  
350 energetics and geometry of sulfide, sulfite, and sulfate incorporation into apatite: The  
351 thermodynamic basis for using this system as an oxybarometer. *Am. Mineral.* **102**, 1646-  
352 1656 (2017).
- 353
- 354 43. Tartèse, R., Anand, M., Joy, K. H. & Franchi, I. A. H and Cl isotope systematics of  
355 apatite in brecciated lunar meteorites Northwest Africa 4472, Northwest Africa 773, Sayh  
356 al Uhaymir 169, and Kalahari 009. *Meteorit. Planet. Sci.* **49**, 2266-2289 (2014).
- 357
- 358 44. McCubbin, F. M. et al. Hydrous melting of the martian mantle produced both depleted  
359 and enriched shergottites. *Geology* **40**, 683-686 (2012).
- 360

## 361 **Methods**

362 **Scanning electron microscopy.** Thin section samples were coated with ~20 nm of carbon prior to  
363 characterisation and mineral identification with the FEI Quanta 3D Dual beam Scanning Electron  
364 Microscope (SEM) fitted with Oxford Instruments X-ray detector at The Open University. X-ray maps  
365 were created with an accelerating voltage of 20.05 kV and a current of ~0.6 nA. High resolution  
366 backscatter electron (BSE) and secondary electron images of regions that included phosphates were

367 acquired for NanoSIMS analysis. The Deben Centaurus cathodoluminescence panchromatic detector  
368 with Hamamatsu Photo Multiplier Tube (fitted to the FEI scanning electron microscope) at The Open  
369 University, with an accelerating voltage of 7 kV – 10 kV and an incident electron beam with a current  
370 of 0.7 nA – 1.5 nA, was used to determine whether zoning and/ or micro-textures in lunar apatite  
371 displayed any quantitative chemical relationship with lunar volatiles (e.g. S and Cl).

372

373 **Ion microprobe analysis.** The Cameca NanoSIMS 50L at The Open University was used for all  
374 abundance and isotope analyses. Measurement of S and Cl abundances and isotopes in the apatite grains  
375 of lunar meteorite SaU 169 were performed before measuring any of the apatite grains in the Apollo  
376 samples to ensure that the modified NanoSIMS S and Cl protocols adopted for this study were feasible  
377 and would result in worthwhile and reproducible volatile measurement results.

378 Imaging mode was used throughout this study because of the heterogeneous nature of apatite grains  
379 with respect to S and Cl. Likewise, imaging ensured that S hotspots (not native to apatite) present within  
380 the apatite grains that contained incredibly high S abundances (many thousands of ppm S) could be  
381 identified and avoided (Supplementary Information).

382 The Cl protocol adopted for this study was based on a modified, existing Cl protocol<sup>27,43</sup>. A Cs<sup>+</sup> primary  
383 beam with a probe current of ~200 pA was used to ‘pre-sputter’ target surfaces to remove gold coating  
384 and any surface contamination by rastering the beam over a 12 µm x 12 µm or 15 µm x 15 µm area for  
385 ~3-5 minutes. The rastered area was reduced to 10 µm x 10 µm and a 20-25 pA Cs<sup>+</sup> primary beam was  
386 used for sample analysis. Negative secondary ions of <sup>18</sup>O, <sup>32</sup>S, <sup>34</sup>S, <sup>35</sup>Cl, <sup>37</sup>Cl and <sup>40</sup>Ca<sup>16</sup>O were collected  
387 simultaneously in multi-collection mode on electron multipliers. The mass resolving power (MRP) was  
388 set to ~8,000 (Cameca definition), enough to resolve interference of <sup>19</sup>F<sup>16</sup>O on <sup>35</sup>Cl. Each imaging  
389 analysis consisted of 50-200 frames, and a frame size of 256 x 256 pixels was used for all images with  
390 an integration time of 500 µs per pixel, leading to total analysis time of 30 minutes to 2 hours.

391 The S protocol involved modifying the Cl protocol and, initially, the NanoSIMS was set up to  
392 simultaneously collect the negative secondary ions of <sup>18</sup>O, <sup>31</sup>P, <sup>32</sup>S, <sup>33</sup>S, <sup>34</sup>S, and <sup>40</sup>Ca<sup>16</sup>O on electron  
393 multipliers but, to counteract the tremendous ionisation of the sample surface caused by very high  
394 counts of <sup>31</sup>P reaching the detector, <sup>31</sup>P was removed and the collected negative secondary ions became

395  $^{18}\text{O}$ ,  $^{32}\text{S}$ ,  $^{33}\text{S}$ ,  $^{34}\text{S}$ ,  $^{35}\text{Cl}$  and  $^{40}\text{Ca}^{16}\text{O}$  (substituting  $^{35}\text{Cl}$  for  $^{37}\text{Cl}$  whenever the counts of  $^{35}\text{Cl}$  became too  
396 high relative to  $^{32}\text{S}$ ). The rastered area was reduced to  $10\ \mu\text{m} \times 10\ \mu\text{m}$  and a 2-40 pA  $\text{Cs}^+$  primary beam  
397 was used for analysis. MRP of  $\sim 11,000$  (Cameca definition) was used to resolve interferences such as  
398  $^{31}\text{PH}$  (on  $^{32}\text{S}$ ),  $^{32}\text{SH}$  (on  $^{33}\text{S}$ ),  $^{32}\text{SH}_2$  and  $^{33}\text{SH}$  (on  $^{34}\text{S}$ ). The imaging conditions were the same as the Cl  
399 imaging analyses, and the typical analysis time varied from  $\sim 1$  to  $\sim 5$  hours (amounting to 100 to 500  
400 frames), where longer times were necessary due to low count rates of  $^{32}\text{S}$ . To offset any positive  
401 electrical charge, an electron flood gun (e-gun) was used during both Cl and S analyses to stabilise the  
402 counts reaching the detectors and reduce the background contribution.

403

404 *Calibration and uncertainty derivation.* Terrestrial reference apatites, including Ap003, Ap004, Ap005  
405 and Ap018 (ref. 44), with known volatile abundances (Francis McCubbin (Johnson Space Centre, *pers.*  
406 *comm.*)) were used during the NanoSIMS analytical sessions to calibrate the unknown volatile  
407 abundances and correct for instrumental mass fractionation. A nominally anhydrous ('dry') San Carlos  
408 olivine reference standard was also used to assess and correct for the total instrumental S and Cl  
409 background contribution.

410 The average  $^{34}\text{S}/^{32}\text{S}$  or  $^{37}\text{Cl}/^{35}\text{Cl}$  ratios of the reference apatite (Ap003 or Ap004, respectively) measured  
411 within a 24 hour period was used to correct the measured  $^{34}\text{S}/^{32}\text{S}$  ratio or  $^{37}\text{Cl}/^{35}\text{Cl}$  ratio of the sample  
412 for IMF within the same period. The typical reproducibility of the  $^{34}\text{S}/^{32}\text{S}$  or  $^{37}\text{Cl}/^{35}\text{Cl}$  ratios of the  
413 reference apatites was  $\sim 0.2\text{‰}$  and  $\sim 0.4\text{‰}$ , respectively. The ratios were then referenced to the known  
414  $\delta^{34}\text{S}_{(\text{V-CDT})}$  values of Durango (Ap003) ( $+0.34\text{‰} \pm 0.02\text{‰}^{21}$ ) and the known  $\delta^{37}\text{Cl}_{(\text{SMOC})}$  of Ap004  
415 ( $+0.11\text{‰}^{27}$ ). The standard deviation of daily measurements of the reference apatites were used to assign  
416 a per mil reproducibility to the isotope values derived for the samples. To calculate the total uncertainty,  
417 error propagation was used to combine the external reproducibility of the reference apatite with the  
418 internal uncertainty of the analytical measurements.

419

420 **X-ray absorption near-edge structure spectroscopy.** The microfocus spectroscopy beamline, I18, at  
421 Diamond Light Source (DLS), Harwell Science and Innovation Campus, UK, was used to collect X-  
422 ray absorption near-edge structure (XANES) spectra at the S K-edge from lunar apatite samples.

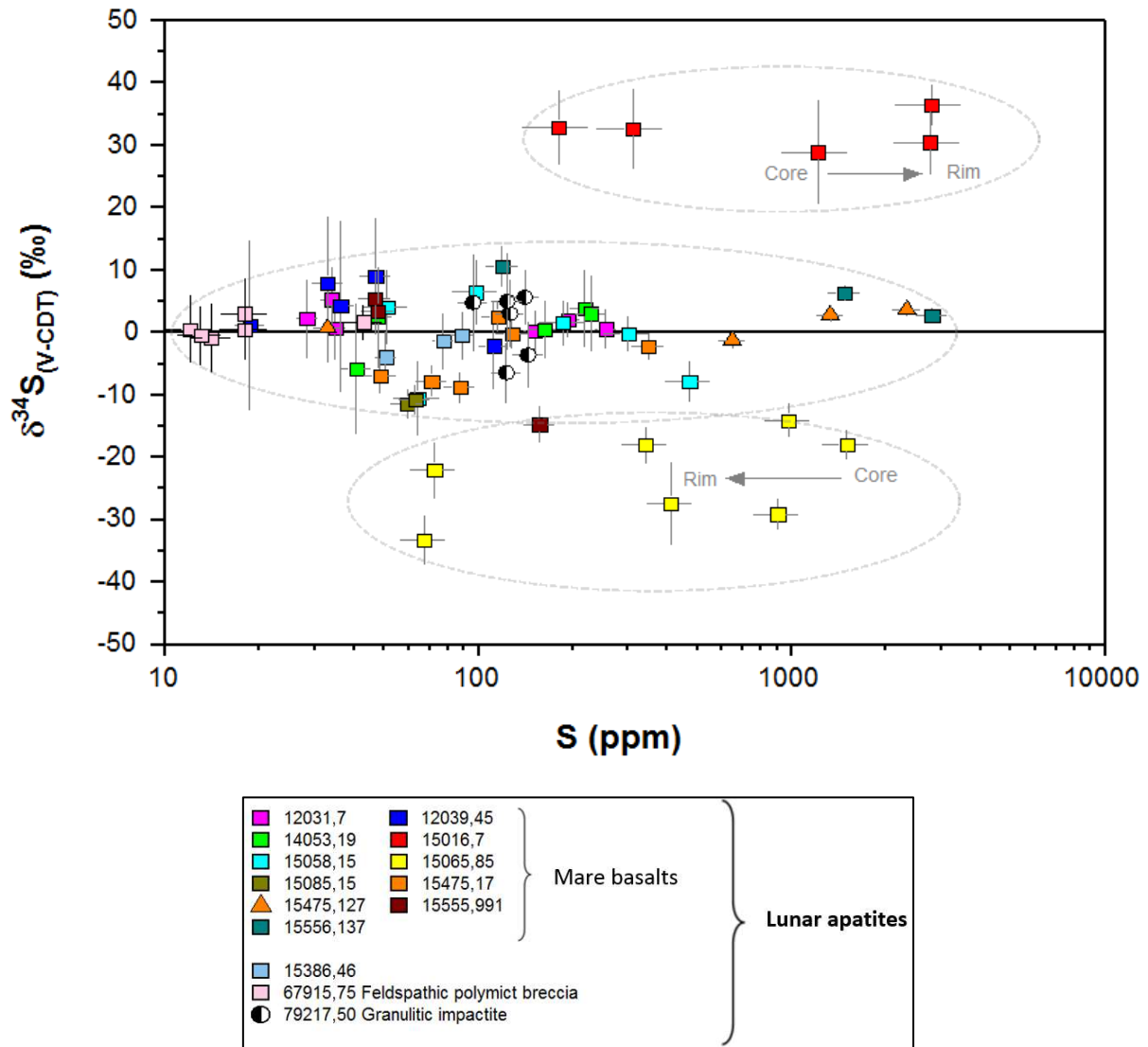
423 S-XANES spectra was collected in fluorescence mode for all analytical sessions with a four-element  
424 Vortex Silicon Drift X-ray detector. Analytical sessions began with S-XANES of the sulfur reference  
425 standards to check the sulfate ( $S^{6+}$ ), sulfite ( $S^{4+}$ ) and sulfide ( $S^{2-}$ ) peak energy positions of the standards  
426 against the corresponding known peak energy positions ( $\sim 2483$  eV,  $\sim 2478$  eV and  $\sim 2470$ , respectively)  
427 (European Synchrotron Radiation Facility (ESRF) database). The Si (111) double crystal  
428 monochromator was used for all S-XANES spectroscopy. All analyses were performed in a helium  
429 environment to minimize absorption of the X-ray fluorescence signal into the surrounding atmosphere.  
430 Kapton tape ( $\sim 13$   $\mu\text{m}$ ) was placed in front of the detector in order to dampen the high phosphorous  
431 signal given off by the apatites. X-ray fluorescence (XRF) element maps of sample regions of interest  
432 (ROI) (typically  $100$   $\mu\text{m}$  x  $100$   $\mu\text{m}$  in size, depending on the apatite grain size) were acquired by  
433 recording fluorescence at  $2500$  eV with a dwell time of  $\sim 0.5$  s per spot. The elements collected were P,  
434 S, Si and Cl (with K-alpha X-ray absorption energies of  $\sim 2013$  eV,  $\sim 2306$  eV,  $\sim 1740$  eV and  $\sim 2620$  eV,  
435 respectively). Analysis points were positioned across the apatite grains with use of the maps to avoid  
436 cracks in the apatite grains and any adjacent areas containing sulfides. S-XANES data was not collected  
437 for some grains due to the close proximity to troilite ( $\text{FeS}^{2-}$ ).

438 A beam size of  $\sim 2$   $\mu\text{m}$  x  $2$   $\mu\text{m}$  and an incident beam intensity (flux) at the S K-edge of  $\sim 1 \times 10^{10}$   
439 photons/s was used for analysis. Initially, XANES spectra included the extended X-ray absorption fine  
440 structure (EXAFS) region by scanning the incident beam from  $2430$  eV to  $2600$  eV, with energy step  
441 sizes of between  $1$  eV and  $5$  eV in the (extended) pre- and post-edge regions and  $0.2$ – $0.5$  eV between  
442  $2465$  eV and  $2507$  eV (which included the S K-edge region of  $\sim 2465$ – $2484$  eV) with scan durations of  
443  $1$  s per energy step. It became apparent that some S in lunar apatites was being oxidized due to the long  
444 scanning range used for S-XANES. This was detected by monitoring the  $S^{6+}$  peak relative to the  $S^{2-}$   
445 peak when making repeat measurements on the same spot on an apatite grain. To address the possibility  
446 of beam damage, the energy range was restricted so that S-XANES spectra were collected by scanning  
447 the incident beam from  $2465$  eV to  $2494$  eV with energy steps of  $0.5$  eV and  $1$  s per energy step.

448  
449  
450

451 **Figures**

452

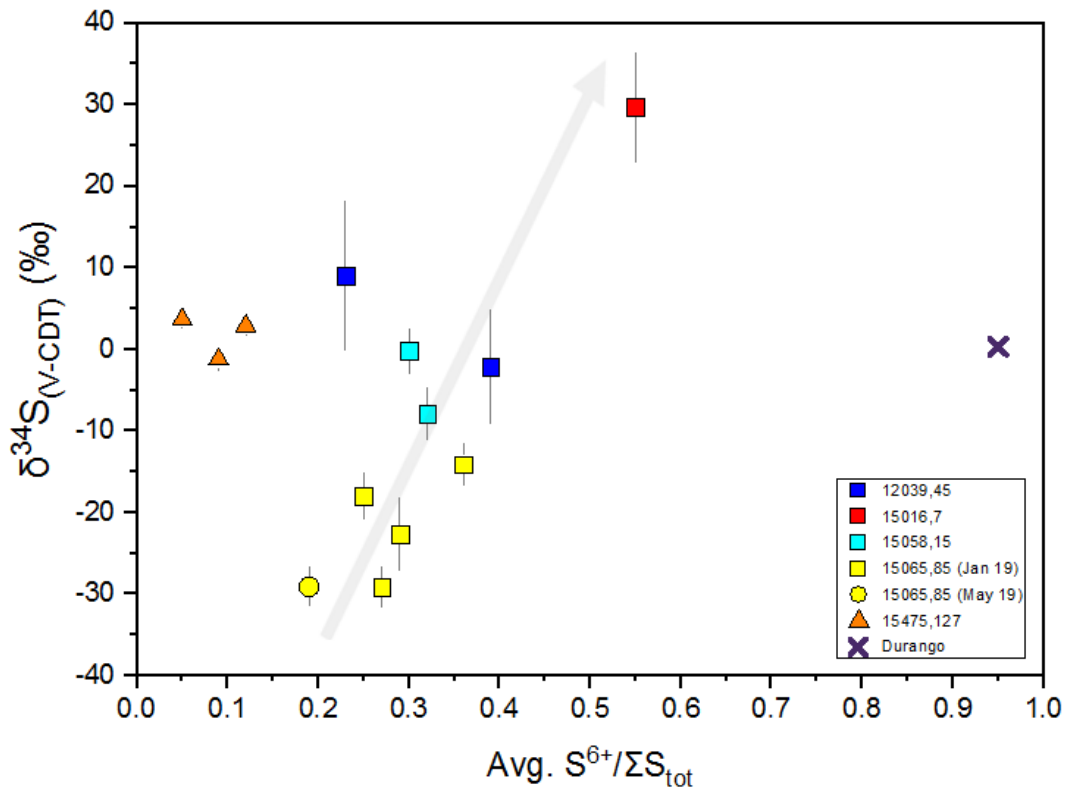


453

454

455 **Figure 1.** Plot of S isotopes ( $\delta^{34}\text{S}_{(\text{V-CDT})}$ ) against S abundance (ppm) in apatite for the analysed lunar  
 456 samples. The graph shows the results of S measurements performed with NanoSIMS for ten Apollo  
 457 mare basalts, a KREEP basalt, a feldspathic polymict breccia and a granulitic impactite. Note the log  
 458 scale on the x-axis. The three distinct clusters of S isotope values have been highlighted with dashed  
 459 ovals. Two grey arrows highlight the direction of the apatite core-rim S variations. The error bars are  
 460 at the  $2\sigma$  uncertainty associated with the measurements.

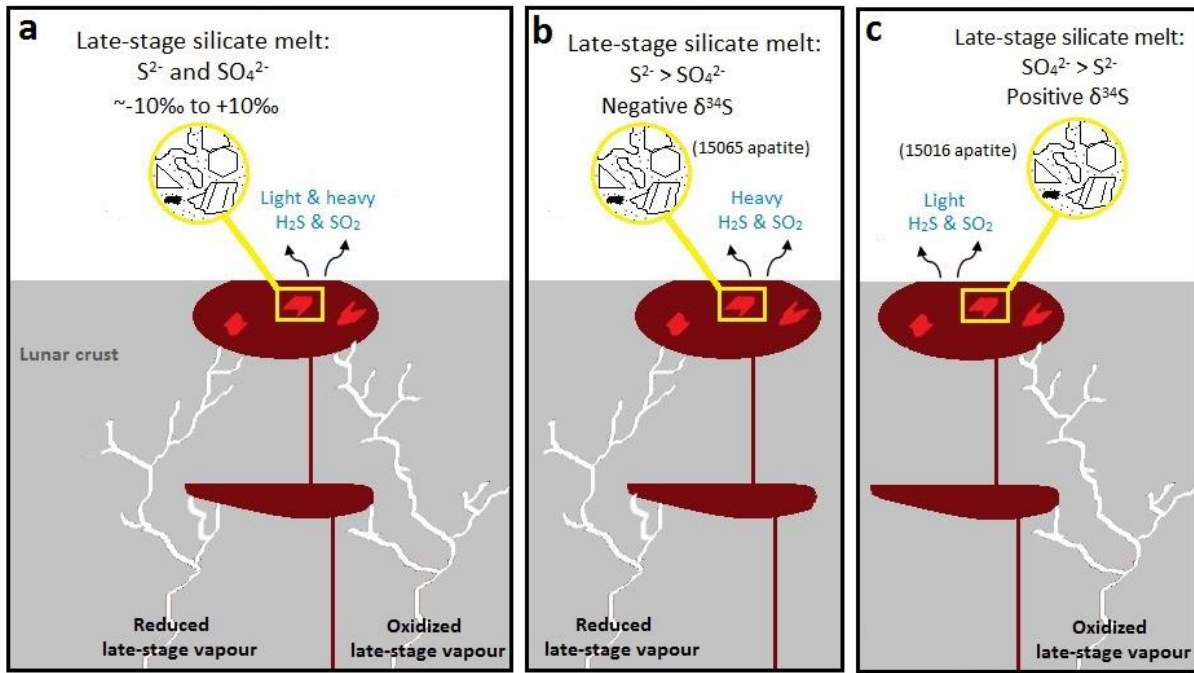
461



462

463 **Figure 2.** Plot of S isotopes ( $\delta^{34}S_{(V-CDT)}$ ) against the average ratio of  $S^{6+}$  to total sulfur ( $S^{6+}/\Sigma S_{tot}$ ) for  
 464 lunar apatites. The individual data points represent the average value of the scans collected for each  
 465 apatite within a specific sample. For the majority of apatites measured, an obvious trend of increasing  
 466  $\delta^{34}S$  with increasing average  $S^{6+}/\Sigma S_{tot}$  is highlighted on the plot (grey arrow) and is typical of that seen  
 467 for terrestrial apatites. By way of comparison, Durango (terrestrial) apatite is also shown  
 468 (Supplementary Information). The  $\delta^{34}S$  error bars represent the standard deviation ( $2\sigma$ ) of the  
 469 measurements made.

470



471

472 **Figure 3.** A cartoon to illustrate various scenarios under which sulfur isotope fractionation might have

473 taken place during late-stage evolution of mare basaltic magmas prior to and during apatite

474 crystallisation. **a**, Shows the typical scenario for samples containing apatites that have (within

475 statistical error)  $\delta^{34}S$  values between  $\sim -10\text{‰}$  and  $\sim +10\text{‰}$ . These apatites may have crystallised from

476 a late-stage silicate melt pocket which was composed of varying quantities of  $S^{2-}$  and  $SO_4^{2-}$ , following

477 interaction with reduced and oxidized late-stage vapour-phases (white veins spreading through lunar

478 crust), mobilised from heterogeneous reservoirs within the lunar crust. For this scenario, both  $^{32}S$  and

479  $^{34}S$  are degassed as  $H_2S$  and  $SO_2$ . **b**, A late-stage silicate melt has interacted with a reduced ( $S^{2-} >$

480  $SO_4^{2-}$ ) late-stage vapour phase and is preferentially degassing  $^{34}S$  (as  $H_2S$  and  $SO_2$ ) to leave the

481 residual melt  $^{32}S$ -rich (e.g. as seen for apatites in sample 15065). **c**, An oxidized late-stage melt ( $SO_4^{2-}$

482  $> S^{2-}$ ) that has formed by interaction with a late-stage oxidized vapour phase and is preferentially

483 degassing  $^{32}S$  (as  $H_2S$  and  $SO_2$ ) to leave the residual melt  $^{34}S$ -rich (e.g. as seen for apatites in sample

484 15016).

# Figures

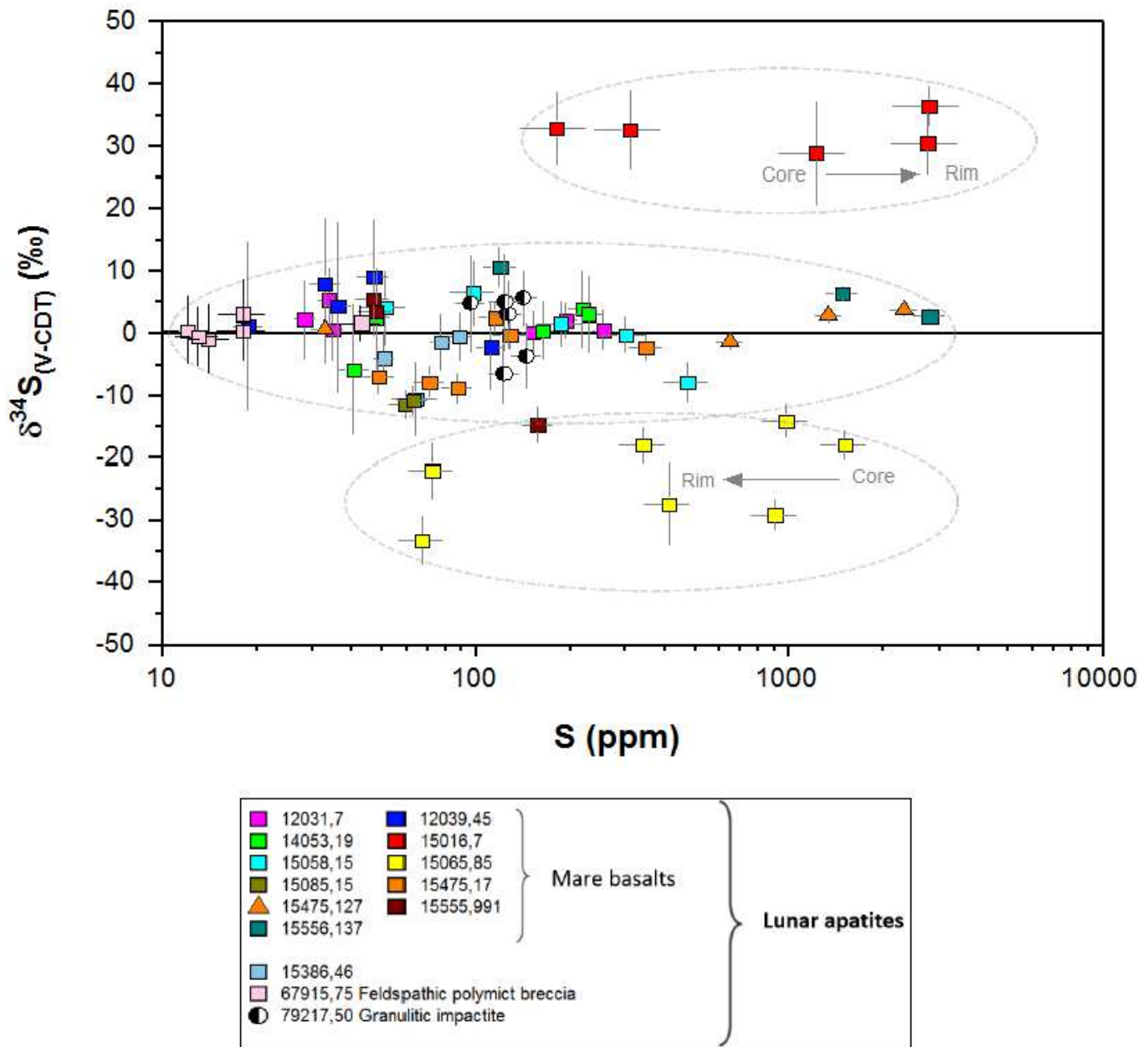


**Figure 1**

Plot of S isotopes ( $\delta^{34}\text{S}_{\text{(V-CDT)}}$ ) against S abundance (ppm) in apatite for the analysed lunar samples. The graph shows the results of S measurements performed with NanoSIMS for ten Apollo mare basalts, a KREEP basalt, a feldspathic polymict breccia and a granulitic impactite. Note the log scale on the x-axis. The three distinct clusters of S isotope values have been highlighted with dashed ovals. Two grey arrows highlight the direction of the apatite core-rim S variations. The error bars are at the  $2\sigma$  uncertainty associated with the measurements.

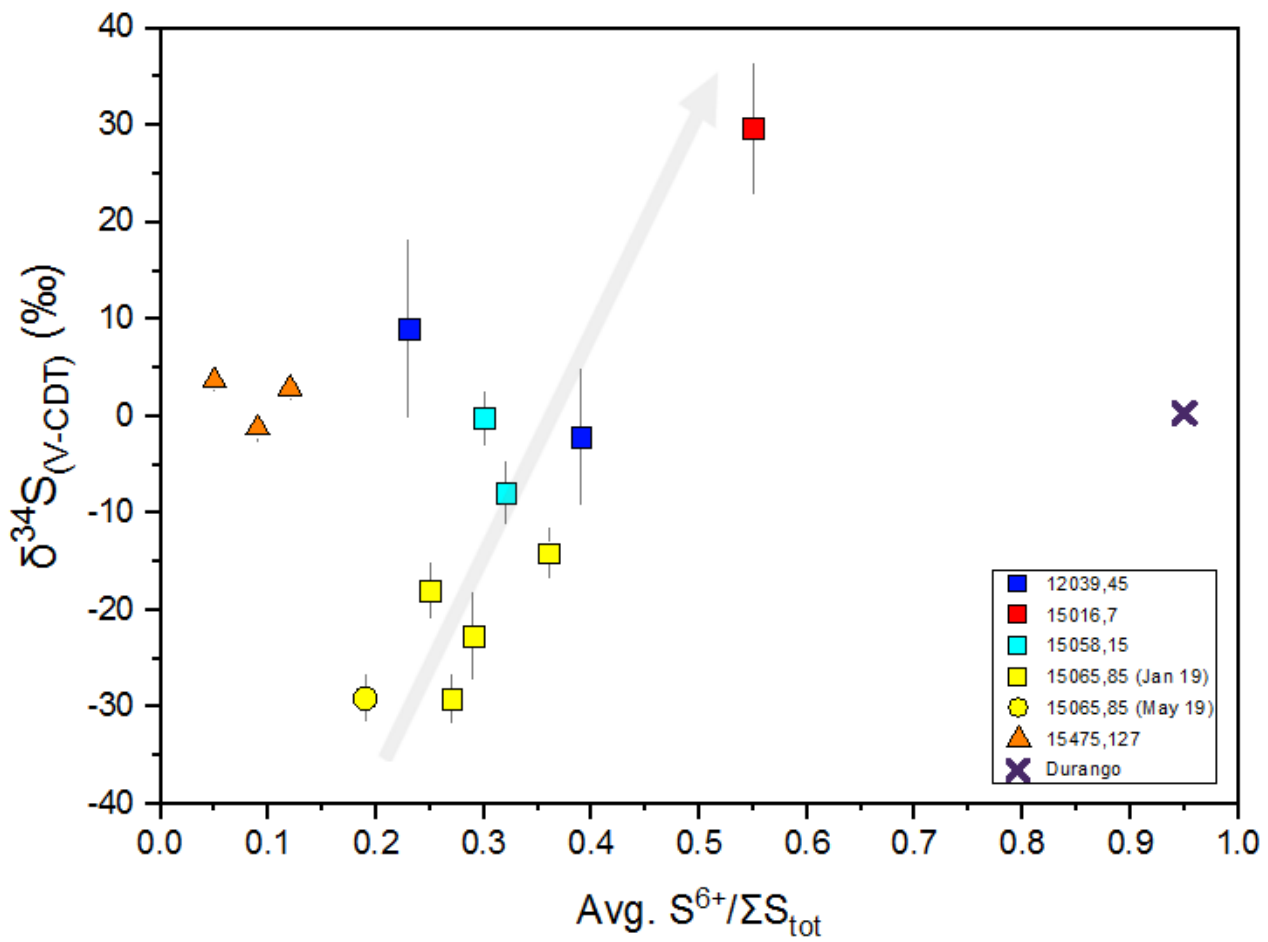


**Figure 2**

Plot of S isotopes ( $\delta^{34}S_{(V-CDT)}$ ) against the average ratio of  $S^{6+}$  to total sulfur ( $S^{6+}/\Sigma S_{tot}$ ) for lunar apatites. The individual data points represent the average value of the scans collected for each apatite within a specific sample. For the majority of apatites measured, an obvious trend of increasing  $\delta^{34}S$  with increasing average  $S^{6+}/\Sigma S_{tot}$  is highlighted on the plot (grey arrow) and is typical of that seen for terrestrial apatites. By way of comparison, Durango (terrestrial) apatite is also shown (Supplementary Information). The  $\delta^{34}S$  error bars represent the standard deviation ( $2\sigma$ ) of the measurements made.

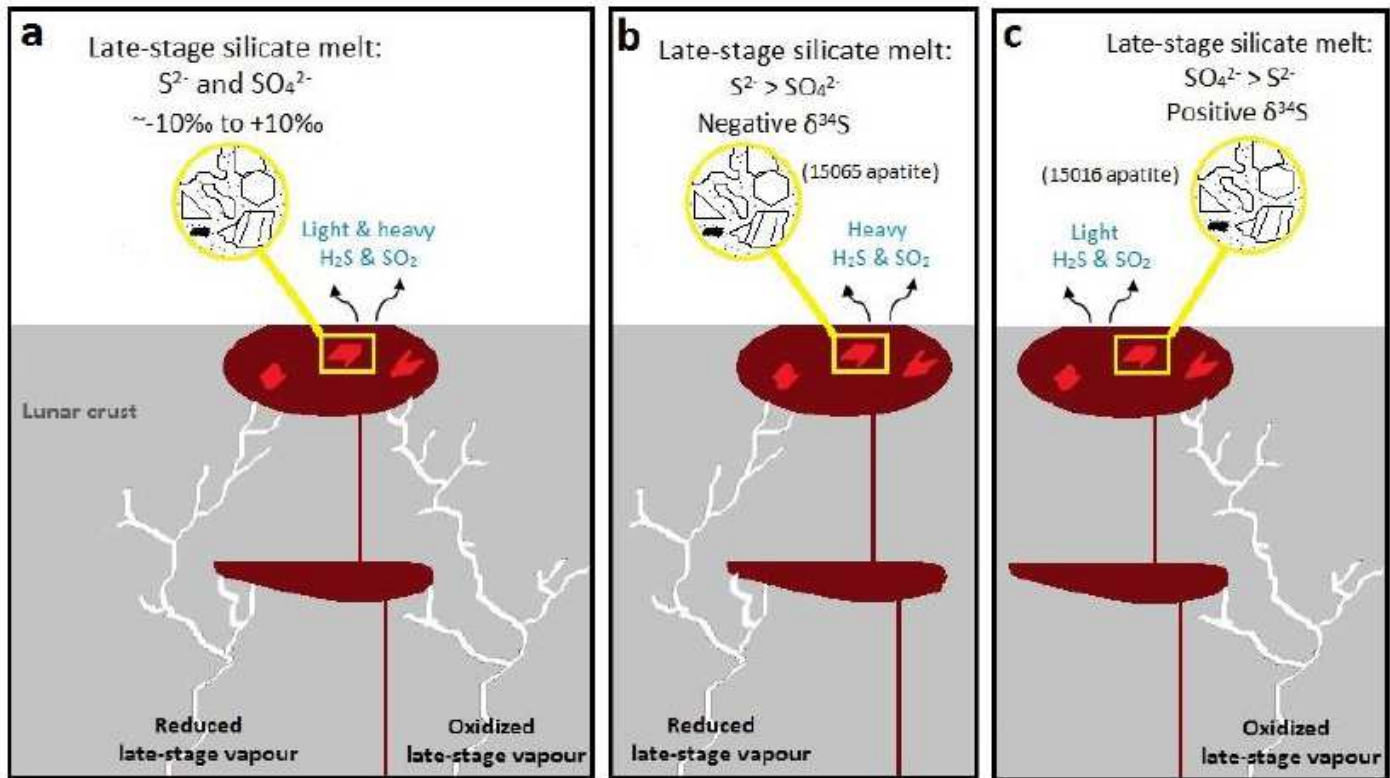


**Figure 3**

A cartoon to illustrate various scenarios under which sulfur isotope fractionation might have taken place during late-stage evolution of mare basaltic magmas prior to and during apatite crystallisation. a, Shows the typical scenario for samples containing apatites that have (within statistical error)  $\delta^{34}S$  values between  $\sim -10\text{‰}$  and  $\sim +10\text{‰}$ . These apatites may have crystallised from a late-stage silicate melt pocket which was composed of varying quantities of  $S^{2-}$  and  $SO_4^{2-}$ , following interaction with reduced and oxidized late-stage vapour-phases (white veins spreading through lunar crust), mobilised from heterogeneous reservoirs within the lunar crust. For this scenario, both  $^{32}S$  and  $^{34}S$  are degassed as  $H_2S$  and  $SO_2$ . b, A late-stage silicate melt has interacted with a reduced ( $S^{2-} > SO_4^{2-}$ ) late-stage vapour phase and is preferentially degassing  $^{34}S$  (as  $H_2S$  and  $SO_2$ ) to leave the residual melt  $^{32}S$ -rich (e.g. as seen for apatites in sample 15065). c, An oxidized late-stage melt ( $SO_4^{2-} > S^{2-}$ ) that has formed by interaction with a late-stage oxidized vapour phase and is preferentially degassing  $^{32}S$  (as  $H_2S$  and  $SO_2$ ) to leave the residual melt  $^{34}S$ -rich (e.g. as seen for apatites in sample 15016).

## Supplementary Files

This is a list of supplementary files associated with this preprint. Click to download.

- [FairclothetalSupplementaryInformation.pdf](#)
- [FairclothetalSupplementaryInformationExcelTables.xlsx](#)